Momentum–density distribution of magnetic electrons in ferromagnetic nickel

2008 J. Phys.: Condens. Matter 20 055201

(http://iopscience.iop.org/0953-8984/20/5/055201)

J. Phys.: Condens. Matter **20** (2008) 055201 (8pp) doi:10.1088/0953-8984/20/05/055201

Momentum–density distribution of magnetic electrons in ferromagnetic nickel

Toshihiro Nagao[1], Yasunori Kubo[2], Akihisa Koizumi[1], Hisao Kobayashi[1], Masayoshi Itou[3] and Nobuhiko Sakai[1]

[1] Graduate School of Material Science, University of Hyogo, Japan
[2] Department of Physics, College of Humanities and Sciences, Nihon University, Japan
[3] Japan Synchrotron Radiation Research Institute (JASRI), SPring-8, Japan

E-mail: toshi_n@sci.u-hyogo.ac.jp

Received 30 August 2007, in final form 21 November 2007
Published 8 January 2008
Online at stacks.iop.org/JPhysCM/20/055201

Abstract

Experimental and theoretical investigations have been made for the first time on the three-dimensional momentum–density distribution of magnetic electrons in ferromagnetic Ni, $\rho_{\rm mag}(\boldsymbol{p})$, which is the difference in the electron momentum–density distribution between majority- and minority-spin electrons. A magnetic Compton-scattering technique is used to determine $\rho_{\rm mag}(\boldsymbol{p})$ by applying the direct Fourier-transform method to reconstruct $\rho_{\rm mag}(\boldsymbol{p})$ from magnetic Compton profiles. The corresponding theoretical $\rho_{\rm mag}(\boldsymbol{p})$ is calculated by the full-potential linearized augmented plane-wave method. The present theory accurately reproduces the overall structures of experimental $\rho_{\rm mag}(\boldsymbol{p})$. There are, however, slight quantitative discrepancies between the experimental and calculated values of $\rho_{\rm mag}(\boldsymbol{p})$ around $|\boldsymbol{p}| = 0$ au and at the positions related to the X-point. The analysis of $\rho_{\rm mag}(\boldsymbol{p})$ for individual bands attributes negative $\rho_{\rm mag}(\boldsymbol{p})$ near the first Brillouin zone boundary ($|\boldsymbol{p}| \sim 1.0$ au) to the superposition of highly negative spin-polarized momentum–density of the first band and highly positive spin-polarized momentum–density of the sixth band. The positively polarized momentum–density at $|\boldsymbol{p}| \sim 2.2$ au is attributed to the d-like fifth band spin polarizations.

1. Introduction

Since the 1960s, 3d transition metals have been studied intensively to understand their electronic structures, which are characterized by hybridization between itinerant s-, p- and nearly localized d-like bands [1]. For magnetic 3d transition metals, the exchange interaction splits electronic states into majority- and minority-spin bands and introduces spin-dependent Fermi surfaces. Thus, their electronic structures become more complicated than those of non-magnetic 3d transition metals. For studies of the band structures of ferromagnetic material, a measurement of momentum–density distribution of magnetic electrons, $\rho_{\rm mag}(\boldsymbol{p})$, is useful because $\rho_{\rm mag}(\boldsymbol{p})$ reflects the spin polarization of all occupied electronic states in a straightforward manner, and is related to spin-dependent momentum–space wavefunctions. A magnetic Compton profile (MCP) measurement is unique in that MCP is the projection of $\rho_{\rm mag}(\boldsymbol{p})$ on the x-ray scattering vector. Thus, MCP measurements have been frequently performed to observe spin-dependent electronic states in ferromagnetic material.

MCP, symbolized by $J_{\rm mag}(p_z)$, is defined as follows ($\hbar = 1$):

$$J_{\rm mag}(p_z) = \int_{-\infty}^{\infty}\int_{-\infty}^{\infty} \rho_{\rm mag}(\boldsymbol{p})\,{\rm d}p_x\,{\rm d}p_y, \tag{1.1}$$

$$\rho_{\rm mag}(\boldsymbol{p}) = \rho_{\uparrow}(\boldsymbol{p}) - \rho_{\downarrow}(\boldsymbol{p}). \tag{1.2}$$

Here, $\rho_{\uparrow}(\boldsymbol{p})$ and $\rho_{\downarrow}(\boldsymbol{p})$ denote the momentum densities of majority- and minority-spin electrons, respectively, and the z-axis direction is taken to be parallel to the x-ray scattering vector. An integrated value of $J_{\rm mag}(p_z)$ over p_z is the spin magnetic moment of the sample. In the following, $\boldsymbol{p}$ will be expressed in atomic units (au) (1 au $= 1.99 \times 10^{-24}$ kg m s^{-1}). It is possible to image $\rho_{\rm mag}(\boldsymbol{p})$ from a finite number of directional $J_{\rm mag}(p_z)$ values with a reconstruction scheme [2]. The so-called direct Fourier-transform method is reported as one of the useful reconstruction schemes [3, 4]. In this reconstruction procedure, first, we evaluate the reciprocal form

factor, $B_{\mathrm{mag}}(0,0,z)$, by the Fourier transform of $J_{\mathrm{mag}}(p_z)$:

$$B_{\mathrm{mag}}(0,0,z) = \int J_{\mathrm{mag}}(p_z)\exp(-\mathrm{i}p_z z)\,\mathrm{d}p_z = \int \rho_{\mathrm{mag}}(\boldsymbol{p})\exp(-\mathrm{i}p_z z)\,\mathrm{d}\boldsymbol{p}. \quad (1.3)$$

When $B_{\mathrm{mag}}(0,0,z)$ values are prepared along various x-ray scattering vectors, a three-dimensional (3D) reciprocal form factor, $B_{\mathrm{mag}}(\boldsymbol{r})$, is obtained by interpolation at fine mesh points in $\boldsymbol{r}$ space. Finally, we obtain $\rho_{\mathrm{mag}}(\boldsymbol{p})$ by the inverse Fourier transform of $B_{\mathrm{mag}}(\boldsymbol{r})$:

$$\rho_{\mathrm{mag}}(p) = \frac{1}{(2\pi)^3}\int B_{\mathrm{mag}}(\boldsymbol{r})\exp(\mathrm{i}\boldsymbol{p}\cdot\boldsymbol{r})\,\mathrm{d}\boldsymbol{r}. \quad (1.4)$$

This method was applied to ferromagnetic Fe + 3 wt% Si, using $J_{\mathrm{mag}}(p_z)$ values along 14 directions [5]. It was found that $\rho_{\mathrm{mag}}(\boldsymbol{p})$ calculated with the full-potential linearized augmented plane-wave method, based on the local spin-density approximation (FLAPW-LSDA) accurately reproduces the experimental values, and assigns the observed negative spin-polarized region in the first Brillouin zone (BZ) to the s- and p-like first and third bands, and positive spin-polarized peaks in high-momentum regions to d-like fourth and fifth bands.

Compared to Fe, Ni exhibits many differences in its electronic structure, resulting from the differences in the crystal structure and number of electrons per atom. For example, the density of states, the bandwidth and the position of the Fermi level all differ. The d-electron density is higher in Ni than in Fe; therefore, the interaction between d-electrons is expected to be stronger in Ni than in Fe and the occupation-number density deviates more from the step function to the non-unity and non-zero densities in $\boldsymbol{k}$-space. Because of these features, it is interesting to examine how accurately the band theory can explain the experimental momentum–density distribution in Ni. Several directional $J_{\mathrm{mag}}(p_z)$ values on ferromagnetic Ni have been measured to be consistent with each other within statistical accuracy, and compared with theoretical values using the band theories with FLAPW-LSDA and the linear muffin-tin orbital method within both LSDA and the generalized gradient approximation [6–8]. It was pointed out that the band calculation with FLAPW-LSDA has provided a better description of the experimental $J_{\mathrm{mag}}(p_z)$, since FLAPW-LSDA calculation produced a value for the spin-magnetic moment closer to the experimental value [7]. The studies revealed that the Umklapp processes in $J_{\mathrm{mag}}(p_z)$, which are derived from both the nature of the wavefunctions and the geometry of the Fermi surface, and appear as fine structures in the high-momentum region of $J_{\mathrm{mag}}(p_z)$, are not as prominent as the theories predicted [7, 8]. Theoretical analyses of MCPs of Ni for individual bands suggested that the contribution from the d-like fifth band to $J_{\mathrm{mag}}(p_z)$ is overestimated [7, 8]. The studies also revealed that, for $|\boldsymbol{p}| < 1$ au, the experimental $J_{\mathrm{mag}}(p_z)$ along the [100] direction has a dip that is deeper than the predicted value from theory [7, 8]. Besides these discrepancies between the experimental and theoretical values of $J_{\mathrm{mag}}(p_z)$, there is controversy about the presence of hole pockets at the X-point. An angle-resolved photoemission spectroscopy study suggests the presence of $X_{5\downarrow}$- and $X_{2\downarrow}$-hole pockets [9], while a study by the de Haas–van Alphen effect indicates the absence of $X_{2\downarrow}$-hole pockets [10]. The LDA + U calculation by Yang *et al* [11] predicts the presence of $X_{5\downarrow}$-hole pockets and the absence of $X_{2\downarrow}$-hole pocket.

In this paper, an experimental $\rho_{\mathrm{mag}}(\boldsymbol{p})$ of Ni is reconstructed from directional $J_{\mathrm{mag}}(p_z)$ values by the direct Fourier-transform method and compared with a theoretical $\rho_{\mathrm{mag}}(\boldsymbol{p})$, calculated with FLAPW-LSDA. Theoretical spin-dependent momentum densities of individual bands are also presented. The hole-pocket controversy mentioned above is examined in the expectation that positively polarized densities may appear at hole-pocket positions in the experimental $\rho_{\mathrm{mag}}(\boldsymbol{p})$.

2. Computations

In the independent particle approximation, the momentum–density is expressed as ($\hbar = 1$)

$$\rho_\sigma(\boldsymbol{p}) = \sum_b \rho_\sigma^b(\boldsymbol{p}) + \rho_\sigma^c(\boldsymbol{p}), \quad (2.1)$$

$$\rho_\sigma^b(\boldsymbol{p}) = \sum_{\boldsymbol{k}} \left|\chi_{\sigma,b,k}(\boldsymbol{p})\right|^2 \theta(E_{\mathrm{F}} - \varepsilon_{\sigma,b,k}), \quad (2.2)$$

with

$$\chi_{\sigma,b,k}(\boldsymbol{p}) = \delta(\boldsymbol{k}+\boldsymbol{G}-\boldsymbol{p})\int \psi_{\sigma,b,k}(\boldsymbol{r})\exp(-\mathrm{i}\boldsymbol{p}\cdot\boldsymbol{r})\,\mathrm{d}\boldsymbol{r}. \quad (2.3)$$

Here ρ_σ^b and ρ_σ^c are momentum densities of spin-dependent bth band electrons and core–electron momentum densities, respectively. The symbols $\boldsymbol{k}$, $\boldsymbol{G}$, $\chi_{\sigma,b,k}$ and $\psi_{\sigma,b,k}$ indicate a wavevector, a reciprocal lattice vector, a momentum space and a real-space wavefunction, respectively. The symbols $\theta(E_{\mathrm{F}} - \varepsilon_{\sigma,b,k})$, E_{F} and $\varepsilon_{\sigma,b,k}$ are a step function, the Fermi energy and the electron energy, respectively.

In the present study, the electronic structure of ferromagnetic Ni has been calculated, based on the FLAPW method in a scalar relativistic version. The exchange–correlation effects have been incorporated within the von Barth–Hedin LSDA scheme [12]. The energy values and wavefunctions have been calculated at 505 $\boldsymbol{k}$-points in the irreducible 1/48th of the BZ for each spin state. The lattice constant, a, has been set to the experimental value of 6.644 au (1 au = 0.0529 nm) [13]. The inscribed sphere radius chosen in the calculation is 2.349 au. Linear-augmented plane-wave basis functions have been truncated at $|\boldsymbol{k}+\boldsymbol{G}| \leqslant 5.8(2\pi/a)$. In the spherical-harmonics expansions, angular momentum values up to $l_{\max} = 8$ have been taken into account. The values of $\rho_\sigma^b(\boldsymbol{p})$ in (2.2) have been determined for 7497 reciprocal lattice vectors, which include more than 99.9% of band electrons. The value of $\rho_\sigma^c(\boldsymbol{p})$ has been calculated from free-atom wavefunctions obtained using the von Barth–Hedin exchange–correlation potential based on LSDA [12]. A modified tetrahedron scheme has been used for the BZ integration of (1.1) [14]. $\rho_{\mathrm{mag}}(\boldsymbol{p})$ in (1.2) is obtained from the difference in spin-dependent momentum densities between

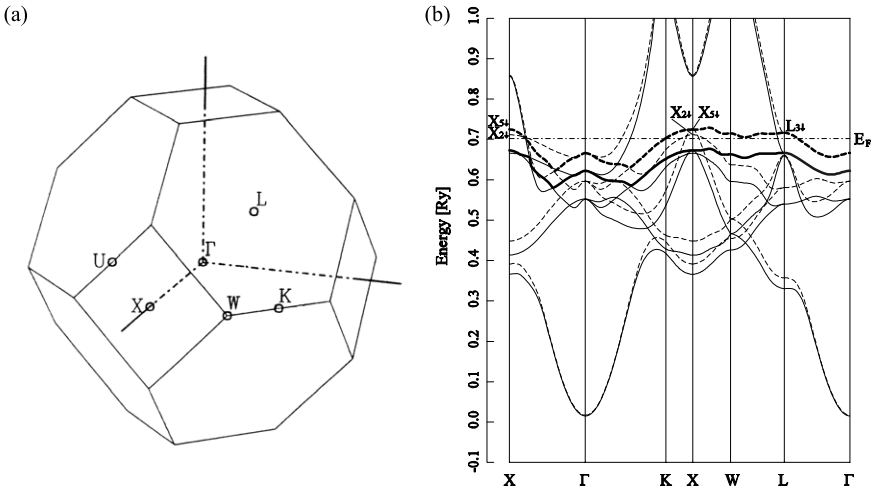

Figure 1. (a) The first BZ of the fcc structure. (b) Energy bands in ferromagnetic Ni, calculated with FLAPW-LSDA. Solid and dashed lines indicate majority- and minority-spin bands, respectively. Thick lines denote the fifth majority- and minority-spin bands. The energy bands are numbered in order of the energy at each $\boldsymbol{k}$-point.

majority-spin ($\sigma = \uparrow$) and minority-spin ($\sigma = \downarrow$) states. The total spin-magnetic moment obtained is $0.565\mu_B$/Ni, in which the spin-magnetic moment from the core electrons is only $-0.0074\ \mu_B$/Ni. The contribution of $\rho^c_{\rm mag}(\boldsymbol{p})$ to the structure of $\rho_{\rm mag}(\boldsymbol{p})$ is negligible. The first BZ of the fcc structure is shown in figure 1(a), and the calculated energy-band diagram is shown in figure 1(b). As seen in the energy-band diagram, the present calculation predicts the $X_{5\downarrow}$-and $X_{2\downarrow}$-hole pockets.

3. Experiment

Three samples of single-crystalline Ni were prepared for 13-directional MCP measurements. The surfaces for each sample were normal to the ⟨001⟩, ⟨110⟩ and ⟨320⟩ directions. A stereographic plot of the 13 directions is shown in figure 2. The MCPs were measured on BL08W at SPring-8, Japan. Elliptically polarized 176 keV x-rays, generated by an elliptical multi-pole wiggler and monochromatized by a bent Si (620) crystal, impinged on the sample with a 0.8 mm × 1 mm spot size. Energy spectra of Compton scattered x-rays, I_+ and I_-, with a scattering angle of 178° were measured with a 10-segmented Ge solid-state detector (Canberra, model GL0115S). The subscript, + or −, denotes whether the direction of an applied magnetic field is parallel or anti-parallel to the scattering vector, respectively. For all the MCP measurements, the magnetic field of 2.5 T was applied to the sample at room temperature. The direction of the magnetic field was alternated in a sequence of '+, −, −, +, −, +, +, −' for 60 s each. It took about 6 h for each MCP measurement. Ordinary data-processing described in [8] was made on I_+ and I_- and $J_{\rm mag}(p_z)$ obtained were folded at $p_z = 0$ au to increase the statistical accuracy. The resultant $J_{\rm mag}(p_z)$ values are shown in figure 3. In each profile, the standard deviation at $p_z = 0$ au is about 3% of $J_{\rm mag}(0)$. Despite Ni having one-third the spin-magnetic moment of Fe, the $J_{\rm mag}(p_z)$ values have been measured with a high statistical accuracy using a state-of-the-art synchrotron-radiation facility.

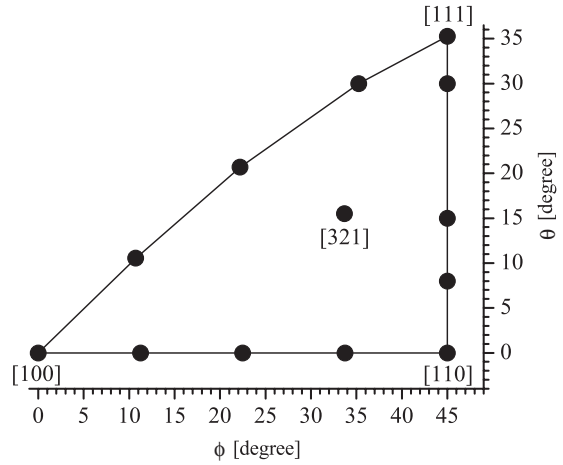

Figure 2. Stereographic plot of 13 measured directions. Symbols ϕ and θ denote the azimuthal and polar angles from the [100] axis, respectively.

The evaluated momentum resolution is 0.52 ± 0.01 au. We have found an excellent agreement between the present and the previous $J_{\rm mag}(p_z)$ values in the [100], [110] and [111] directions [7, 8]. This confirms the reliable reproducibility of the experimental $J_{\rm mag}(p_z)$. The corresponding theoretical $J_{\rm mag}(p_z)$ values are shown by the red lines. The area of each experimental $J_{\rm mag}(p_z)$, between $p_z = -10$ au and +10 au, is normalized to the theoretical spin-magnetic moment of Ni.

4. Results and discussion

In figure 3, the 13 experimental $J_{\rm mag}(p_z)$ values are shown together with the theoretical ones which are convoluted with a Gaussian function having a full width at half maximum of the experimental resolution. Although the agreement between the experiment and theory is fairly good, the following discrepancies are recognized. (i) The dip in the experimental

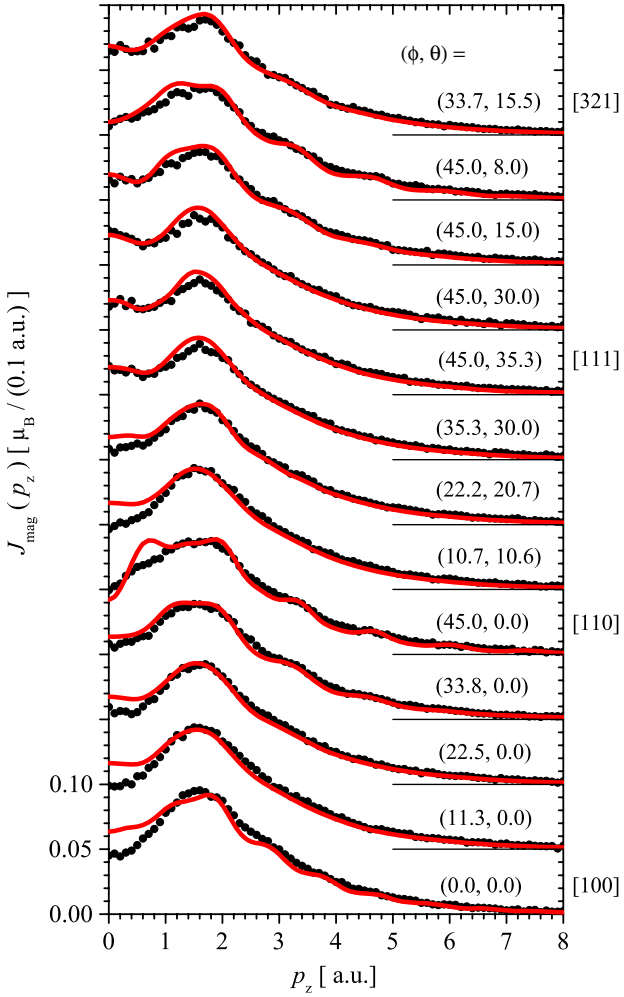

Figure 3. Experimental (solid circles) and theoretical (red lines) $J_{\rm mag}(p_z)$ values of Ni along 13 directions. Theoretical $J_{\rm mag}(p_z)$ values are convoluted with the experimental resolution. The standard deviations are smaller than the size of the solid circles.

$J_{\rm mag}(p_z)$ for $p_z < 1$ au is deeper than that in the theoretical one along the [100] direction. (ii) The theory predicts distinct periodic peaks indicating the Umklapp processes at $p_z \sim 0.7$, 2.0, 3.3 and 4.7 au along the [110] direction, while the experimental $J_{\rm mag}(p_z)$ does not show prominent peaks, especially at $p_z \sim 0.7$ and 2.0 au. (iii) The theory slightly overestimates the peak at $p_z \sim 1.6$ au along the [111] direction. These discrepancies along the [100], [110] and [111] directions have been previously mentioned in reports [7, 8]. Along the other directions, discrepancies similar to (i), (ii) or (iii) are also observed, as shown in figure 3.

The 13 experimental $J_{\rm mag}(p_z)$ values shown in figure 3 have been used to reconstruct $\rho^{(13)}_{\rm mag}(\boldsymbol{p})$, where the superscript denotes the number of $J_{\rm mag}(p_z)$ values for reconstruction. In the direct Fourier-transform procedure, an empirical filter function, defined by equation (4.3) in [4], has been multiplied with $B_{\rm mag}(0, 0, z)$ to reduce the high-frequency components originating from statistical errors in $J_{\rm mag}(p_z)$. The (100) and (110) cross-sections of the experimental $\rho^{(13)}_{\rm mag}(\boldsymbol{p})$ are presented in figures 4(a) and (b), respectively. The first BZ boundary is represented by the solid white lines, and the reciprocal lattice points are marked by the open circles. The BZ boundaries centred at each reciprocal lattice point are indicated by dashed white lines for convenience in the following discussions. Highly negative $\rho^{(13)}_{\rm mag}(\boldsymbol{p})$ are recognized in the vicinity of the first BZ boundary and around $|\boldsymbol{p}| = 0$ au. Outside the first BZ boundary, $\rho^{(13)}_{\rm mag}(\boldsymbol{p})$ increases with increasing $|\boldsymbol{p}|$, and highly positive $\rho^{(13)}_{\rm mag}(\boldsymbol{p})$ appear at $|\boldsymbol{p}| \sim 2.2$ au. In the (110) plane, positive peaks appear in $\rho^{(13)}_{\rm mag}(\boldsymbol{p})$ around the positions denoted by A and B in figure 4(b). The momentum at A, $\boldsymbol{p}_{\rm A}$, is expressed as $\boldsymbol{p}_A = \boldsymbol{k}_{\frac{\bar{1}}{2}\frac{1}{2}\frac{\bar{1}}{2}} + \boldsymbol{G}_{\bar{1}11}$ where $\boldsymbol{k}_{\frac{\bar{1}}{2}\frac{1}{2}\frac{\bar{1}}{2}}$ is the L-point wavevector in the first BZ. The subscripts of $\boldsymbol{k}$ and $\boldsymbol{G}$ denote x, y and z components, in units of $2\pi/a$. The momentum at B, $\boldsymbol{p}_{\rm B}$, is expressed as $\boldsymbol{p}_B = \boldsymbol{k}_{001} + \boldsymbol{G}_{\bar{1}11}$, where $\boldsymbol{k}_{001}$ is the X-point wavevector. A positive peak in $\rho^{(13)}_{\rm mag}(\boldsymbol{p})$ is expected to appear in the (100) plane at positions related to the X-point. In figure 4(a), at the position denoted by C, the momentum, $\boldsymbol{p}_{\rm C}$, is expressed as $\boldsymbol{p}_C = \boldsymbol{k}_{010} + \boldsymbol{G}_{002}$. A positive plateau appears around the position denoted by D in the (100) plane, whereas no positive peak is formed at C.

Theoretical $\rho^{(13)}_{\rm mag}(\boldsymbol{p})$ has been reconstructed from 13 theoretical $J_{\rm mag}(p_z)$ shown in figure 3, by the same procedure utilized for reconstructing the experimental $\rho^{(13)}_{\rm mag}(\boldsymbol{p})$. To verify the adequacy of the reconstruction procedure, theoretical $\rho^{(13)}_{\rm mag}(\boldsymbol{p})$ is compared with original $\rho_{\rm mag}(\boldsymbol{p})$, which is convoluted with a 3D Gaussian function having a full width at half maximum of the experimental resolution. The (100) and (110) cross-sections of both the theoretical $\rho^{(13)}_{\rm mag}(\boldsymbol{p})$ and the convoluted original $\rho_{\rm mag}(\boldsymbol{p})$ are also shown in figures 4(c)–(f). Comparing them shows that theoretical $\rho^{(13)}_{\rm mag}(\boldsymbol{p})$ reproduces all the features of convoluted original $\rho_{\rm mag}(\boldsymbol{p})$ very well, although slight smearing is introduced during the reconstruction process. This indicates that the number and the distribution of the directions along which MCPs are measured are properly chosen to obtain experimental $\rho_{\rm mag}(\boldsymbol{p})$. The theoretical $\rho^{(13)}_{\rm mag}(\boldsymbol{p})$ reproduces highly negative experimental $\rho^{(13)}_{\rm mag}(\boldsymbol{p})$ near the first BZ boundary and positive ones around A and B in the (110) plane. The theoretical $\rho^{(13)}_{\rm mag}(\boldsymbol{p})$ has peaks at C in the (100) plane, whereas the experimental $\rho^{(13)}_{\rm mag}(\boldsymbol{p})$ in figure 4(a) forms no positive peaks at C. The relative amounts of the theoretical $\rho^{(13)}_{\rm mag}(\boldsymbol{p})$ at $\boldsymbol{p}_{\rm A}$, $\boldsymbol{p}_{\rm B}$, $\boldsymbol{p}_{\rm C}$ and $\boldsymbol{p}_{\rm D}$ are approximately 8%, 9%, 9% and 6%, respectively, with respect to the electron momentum–density, $\sum_{b,\sigma} {\rho_\sigma}^b(\boldsymbol{p})$.

Figure 5 shows the experimental $\rho^{(13)}_{\rm mag}(\boldsymbol{p})$ on the [100], [110] and [111] axes, where the error bars denote standard deviations. The propagation of errors in the experimental $J_{\rm mag}(p_z)$ to $\rho^{(13)}_{\rm mag}(\boldsymbol{p})$ through the reconstruction procedure has been analysed according to the formalism in [4]. The evaluation of the standard deviations of $\rho^{(13)}_{\rm mag}(\boldsymbol{p})$ was performed in the (100) and (110) planes. The largest error, 0.0032 $\mu_{\rm B}/(0.1\ {\rm au})^3$, is found at $|\boldsymbol{p}| = 0$ au. The standard deviations along highly symmetrical axes, such as the [100], [110] and [111] axes, are found to be larger than those at other positions, as reported in [4]. The standard deviations at $|\boldsymbol{p}| \sim 1$ au are less than two intervals of the contour shown in figure 4. Thus, the fine structures of the experimental $\rho^{(13)}_{\rm mag}(\boldsymbol{p})$ outside the first BZ are not artefacts. The theoretical $\rho^{(13)}_{\rm mag}(\boldsymbol{p})$ on the [100], [110] and [111] axes is compared with

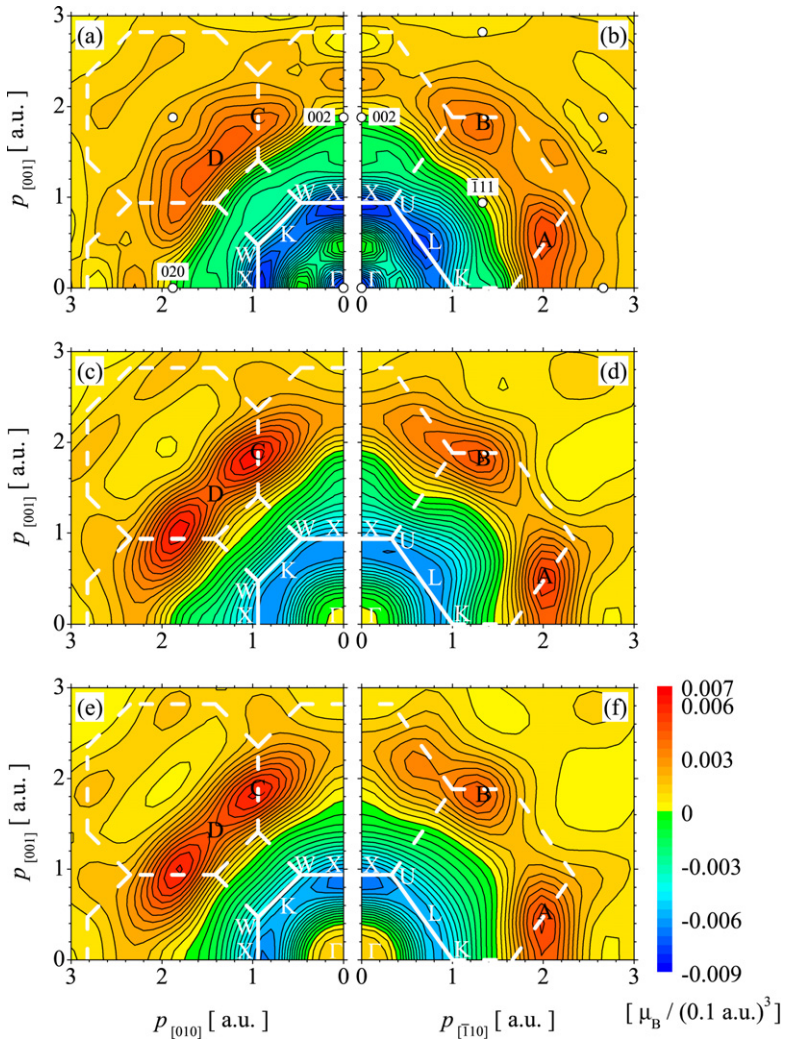

Figure 4. Experimental and theoretical momentum–density distributions of magnetic electrons. Experimental $\rho^{(13)}_{\rm mag}(\boldsymbol{p})$ is shown in (a) for the (100) plane and in (b) for the (110) plane. The contour interval is 0.0005 $\mu_{\rm B}/(0.1\ {\rm au})^3$. White solid lines are the first BZ boundary and some symmetry points are marked with the white letters. For the white dashed lines, see the text. White points are the reciprocal lattice points. The (020), (002) and ($\bar{1}11$) reciprocal lattice points are labelled. Theoretical $\rho^{(13)}_{\rm mag}(\boldsymbol{p})$ is shown in (c) for the (100) plane and in (d) for the (110) plane. Convoluted original $\rho_{\rm mag}(\boldsymbol{p})$ is shown in (e) for the (100) plane and in (f) for the (110) plane.

the experimental data in figure 5. They show good quantitative agreements in the region $|\boldsymbol{p}| > 0.5$ au, while the discrepancy beyond the error bar is clear near $|\boldsymbol{p}| = 0$ au.

Origins of fine structures in $\rho^{(13)}_{\rm mag}(\boldsymbol{p})$ can be clarified using theoretical momentum densities of magnetic electrons of individual bands, $\rho^{b}_{\rm mag}(\boldsymbol{p}) = \rho^{b}_{\uparrow}(\boldsymbol{p}) - \rho^{b}_{\downarrow}(\boldsymbol{p})$. $\rho^{b}_{\rm mag}(\boldsymbol{p})$ has been reconstructed from theoretical 13-directional MCPs for individual bands, convoluted with the experimental momentum resolution, using the same procedure utilized for reconstructing the experimental $\rho^{(13)}_{\rm mag}(\boldsymbol{p})$. Figure 6 shows $\rho^{b}_{\rm mag}(\boldsymbol{p})$ in the (100) and (110) planes. Each $\rho^{b}_{\rm mag}(\boldsymbol{p})$ has characteristic features: $\rho^{\rm 1st}_{\rm mag}(\boldsymbol{p})$ shows highly negative spin polarization in the region of $|\boldsymbol{p}| \sim 0.6$ au, $\rho^{\rm 5th}_{\rm mag}(\boldsymbol{p})$ forms highly positive peaks at $|\boldsymbol{p}| \sim 2.2$ au and $\rho^{\rm 6th}_{\rm mag}(\boldsymbol{p})$ shows highly positive spin polarization in the region of $|\boldsymbol{p}| \sim 0.4$ au. The reason for $\rho^{\rm 1st}_{\rm mag}(\boldsymbol{p})$ showing highly negative spin polarization in the region of $|\boldsymbol{p}| \sim 0.6$ au ($|\boldsymbol{G}| = 0$ region) is as follows. The energy-band diagram in figure 1(b) shows that the states in the first band are composed mostly of s- and p-characteristics around the Γ-point and of d-character near the first BZ boundary, because of the hybridization between s-, p- and d-like bands. The hybridization in the first majority-spin band occurs ahead of the first minority-spin band because the d-like majority-spin bands are lower in energy than the d-like minority-spin bands. Thus, the components of s- and p-characteristics in the first minority-spin band are larger than those in the majority-spin one near the first BZ boundary. In addition, the radial momentum wavefunctions for s- and p-characteristics has large values for $|\boldsymbol{p}| < 1$ au, while that for d-character peaks at $|\boldsymbol{p}| \sim 2$ au. These features can be recognized in figure 7 by the radial momentum wavefunction, $F_l(|\boldsymbol{p}|; E_l)$, which is the Fourier transform of the lth radial wavefunction with the energy E_l in real space [15, 16]: l corresponds to s-, p- or d-character of the real-space wavefunction. Thus the negative $\rho^{\rm 1st}_{\rm mag}(\boldsymbol{p})$ is caused by the hybridization and the difference in $F_l(|\boldsymbol{p}|; E_l)$ between s-, p- and d-states.

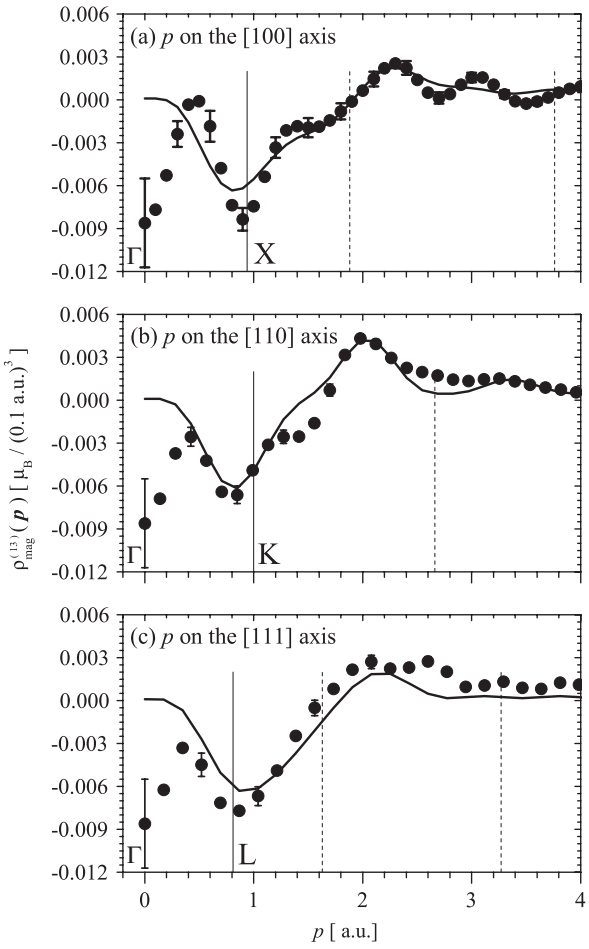

Figure 5. Experimental (solid circles) and theoretical (solid lines) $\rho^{(13)}_{\rm mag}(\boldsymbol{p})$. (a), (b) and (c) are the [100], [110] and [111] axes, respectively. The interval of the subscale, 0.0005 $\mu_{\rm B}/(0.1\ {\rm au})^3$, is equal to the contour interval in figure 4. Vertical solid and dashed lines denote the positions of the symmetry points and reciprocal lattice points, respectively. For the error bars, see the text.

In the case of $\rho^{\rm 6th}_{\rm mag}(\boldsymbol{p})$, the states in the sixth band are composed mostly of d-character around the Γ-point, and s- and p-characteristics increase near the first BZ boundary, as shown in figure 1(b). It is a particular feature of the sixth band that the Fermi surface of the majority-spin band is larger than the surface of the minority-spin band. When $|\boldsymbol{k}|$ is in the region between $|\boldsymbol{k}_F^{\rm min}|$ and $|\boldsymbol{k}_F^{\rm maj}|$, only the states in the majority-spin band contribute to $\rho^{\rm 6th}_{\rm mag}(\boldsymbol{p})$, where $\boldsymbol{k}_{\rm F}^{\rm min}$ and $\boldsymbol{k}_{\rm F}^{\rm maj}$ denote the Fermi wavevectors of the minority- and majority-spin bands, respectively, with the same direction as $\boldsymbol{p}$. This means that $\rho^{\rm 6th}_{\rm mag}(\boldsymbol{p})$ becomes highly positive in this region of $|\boldsymbol{k}_{\rm F}^{\rm min}| < |\boldsymbol{k}| < |\boldsymbol{k}_{\rm F}^{\rm maj}|$ for $\boldsymbol{p} = \boldsymbol{k}$ ($|\boldsymbol{G}| = 0$). Thus, negative $\rho_{\rm mag}(\boldsymbol{p})$ near the first BZ boundary is formed by the superposition of negative $\rho^{\rm 1st}_{\rm mag}(\boldsymbol{p})$ and positive $\rho^{\rm 6th}_{\rm mag}(\boldsymbol{p})$.

Regarding $\rho^{\rm 5th}_{\rm mag}(\boldsymbol{p})$, the situation is very different from those in the first and sixth bands. The fifth majority-spin band is completely filled, while the minority-spin band is partially filled and the dominant states in both bands are of d-character with $3z^2 - r^2$ and $x^2 - y^2$ type symmetries. When $\boldsymbol{k}$ is located in a region where both the majority- and minority-spin bands are occupied, $\rho^{\rm 5th}_{\rm mag}(\boldsymbol{p})$ is nearly zero. When $\boldsymbol{k}$ is located in a region where the minority-spin band is empty, such as near X-, W- and L-points, $\rho^{\rm 5th}_{\rm mag}(\boldsymbol{p})$ forms positive spin polarization, which reflects the position and size of the empty region of the minority-spin band. In addition, the radial momentum wavefunction for d-character peaks at $|\boldsymbol{p}| \sim 2$ au, as mentioned above. Then, the spin polarization of the d-like fifth band peaks at $|\boldsymbol{p}| \sim 2.2$ au and is mainly attributed to positive $\rho_{\rm mag}(\boldsymbol{p})$ at A, B and C. The positive peaks at C in $\rho_{\rm mag}(\boldsymbol{p})$, which indicate the Umklapp processes, are projected on the values of theoretical $J_{\rm mag}(p_z)$ along the [110] axis and form prominent peaks at $p_z = 0.66$ and 1.99 au. This feature induces the discrepancy between the experimental and the theoretical $J_{\rm mag}(p_z)$ along the [110] axis.

The positive $\rho^{(13)}_{\rm mag}(\boldsymbol{p})$ around B, C and D in figures 4(a) and (b) should not be taken as a sign indicating the presence of the $X_{5\downarrow}$- and/or $X_{2\downarrow}$-hole pockets. As seen from the energy band in figure 1(b), the $X_{2\downarrow}$- and $X_{5\downarrow}$-hole pockets belong to the third and the fourth bands, respectively. As seen in figures 6(e)–(j), we find no positive peaks at B and C in $\rho^{\rm 3rd}_{\rm mag}(\boldsymbol{p})$ and $\rho^{\rm 4th}_{\rm mag}(\boldsymbol{p})$. On the other hand, we clearly see positive peaks at B and C in $\rho^{\rm 5th}_{\rm mag}(\boldsymbol{p})$. These features are not due to convolution with the experimental momentum resolution. Even in non-convoluted $\rho^{\rm 3rd}_{\rm mag}(\boldsymbol{p})$ and $\rho^{\rm 4th}_{\rm mag}(\boldsymbol{p})$ the peaks at B and C are too small to be distinguished from the peaks in non-convoluted $\rho^{\rm 5th}_{\rm mag}(\boldsymbol{p})$. Therefore, the positive peaks in $\rho^{(13)}_{\rm mag}(\boldsymbol{p})$ are not a signature of the hole pockets, but related to the large-hole Fermi surface of the fifth minority-spin band. The present analysis of $\rho^{(13)}_{\rm mag}(\boldsymbol{p})$ for individual bands indicates that the presence of the hole pockets of Ni cannot be examined experimentally by MCP measurements.

The origin of the discrepancies between experiment and theory in $\rho^{(13)}_{\rm mag}(\boldsymbol{p})$ around C–D and $|\boldsymbol{p}| = 0$ au may be ascribed to the quasi-particle nature of the electron system, in particular to the non-unity and non-zero occupation in $\boldsymbol{k}$-space. One of the present authors (YK) computed Compton profiles of Cu with the GW approximation (GWA) [17] using FLAPW basis sets and obtained better agreement with the experiment than with results computed with the FLAPW-LDA alone [18]. The GWA scheme, however, does not work well for the MCPs of Ni [19]. Ordinary GWA includes only long-range correlation effects and can work well for Cu because of fully occupied d-like bands. It has been pointed out that, for Ni, the short-range correlation effects are important [20]. Evaluating these effects requires higher-order diagrams in GWA for electron–electron and hole–hole scattering processes.

5. Summary

The momentum–density distribution of magnetic electrons, $\rho_{\rm mag}(\boldsymbol{p})$, of ferromagnetic Ni has been experimentally and theoretically clarified for the first time. Experimental $\rho_{\rm mag}(\boldsymbol{p})$ of Ni has been reconstructed by applying the direct Fourier-transform method to 13-directional experimental $J_{\rm mag}(p_z)$. The experimental results were compared with the theoretical $\rho_{\rm mag}(\boldsymbol{p})$, calculated with the FLAPW method based on the LSDA, and the present theory accurately reproduced the fine

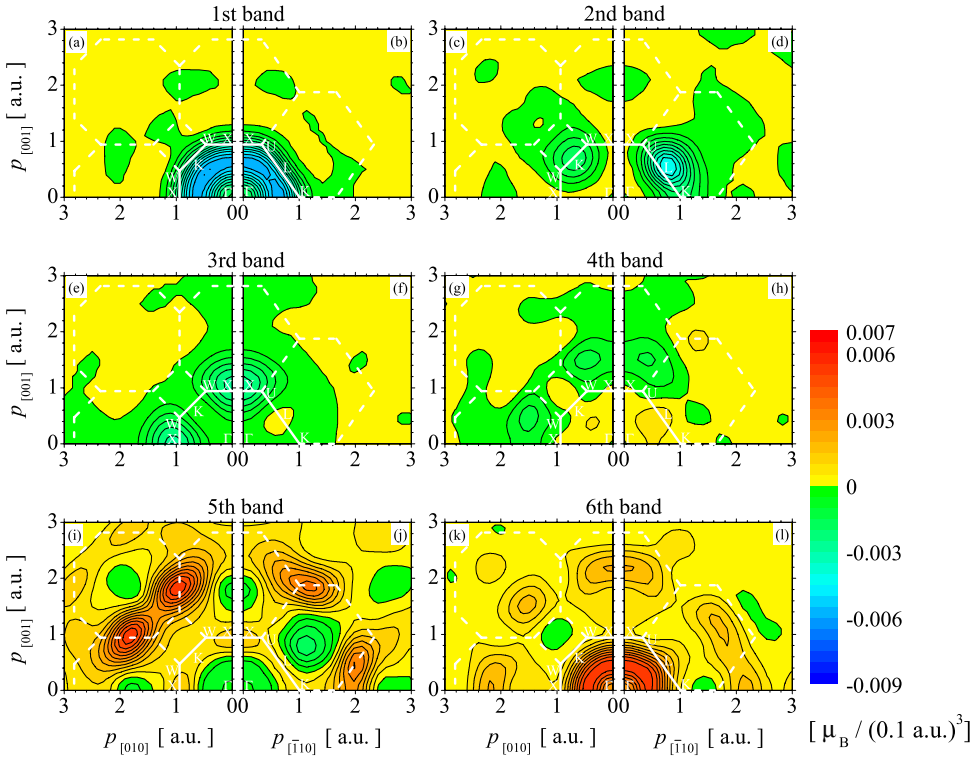

Figure 6. Partial contribution from each band to $\rho^{(13)}_{\rm mag}(\boldsymbol{p})$. The left-hand side is the (100) plane and the right-hand side is the (110) plane. The contour interval is 0.0005 $\mu_B/(0.1{\rm au})^3$. White solid lines are the first BZ boundary. Some symmetry points are marked with white letters. For white dashed lines, see the text.

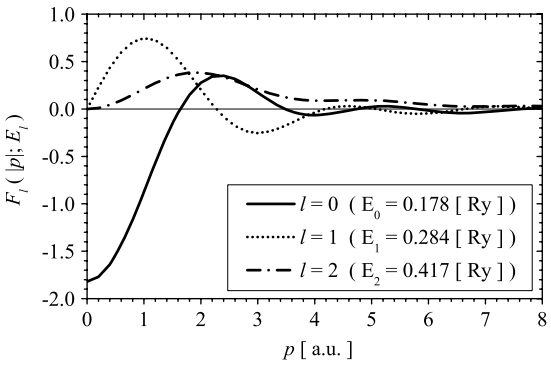

Figure 7. Radial momentum wavefunctions, $F_l(|\boldsymbol{p}|; E_l)$, in majority-spin bands for s-, p- and d-characteristics.

structures of experimental $\rho_{\rm mag}(\boldsymbol{p})$ except around $|\boldsymbol{p}| = 0$ au and at the positions related to the X-point. The analyses of the spin-dependent momentum densities of individual bands are found to be useful in interpreting the experimental $\rho_{\rm mag}(\boldsymbol{p})$. We concluded that: (i) the observed dominant positive $\rho_{\rm mag}(\boldsymbol{p})$ in the high-momentum region mainly originates in d-like fifth band spin polarization and (ii) negative $\rho_{\rm mag}(\boldsymbol{p})$ near the first BZ boundary is interpreted as a result of the superposition of s- and p-like first and sixth band spin polarizations. The present comparison provides a good test for the accuracy of the LSDA applied to the electron system.

Acknowledgments

The authors thank Drs Y Tanaka of RIKEN (the Institute of Physical and Chemical Research) and S Mizusaki of Aoyama Gakuin University for supplying the programs for reconstruction and error propagation, and for useful discussions on the reconstruction procedure. The MCP measurements were performed with the approval of the Japan Synchrotron Research Institute (JASRI) at SPring-8 (No. J05A08W0-0513N and 2006A0097).

References

[1] Wohlfarth E P 1980 *Ferromagnetic Materials* vol 1, ed E P Wohlfarth (Amsterdam: North Holland) pp 1–70
[2] Hansen N K 2004 *X-Ray Compton Scattering* ed M J Cooper *et al* (New York: Oxford University Press) pp 163–87
[3] Suzuki R, Osawa M, Tanigawa S, Matsumoto M and Shiotani N 1989 *J. Phys. Soc. Japan* **58** 3251–63
[4] Tanaka Y, Sakurai Y, Stewart A T, Shiotani N, Mijnarends P E, Kaprzyk S and Bansil A 2001 *Phys. Rev.* B **63** 045120
[5] Tanaka Y, Sakai N, Kubo Y and Kawata H 1993 *Phys. Rev. Lett.* **70** 1537–40
[6] Sakai N, Ito M, Kawata H, Iwazumi T, Ando M, Shiotani N, Itoh F, Sakurai Y and Nanao S 1991 *Nucl. Instrum. Methods Phys. Res.* A **303** 488–94
[7] Dixson M A G, Duffy J A, Gardelis S, McCarthy J E, Cooper M J, Dugdale S B, Jarlborg T and Timms D N 1998 *J. Phys.: Condens. Matter* **10** 2759–71
[8] Kakutani Y, Kubo Y, Koizumi A, Sakai N, Ahuja B L and Sharma B K 2003 *J. Phys. Soc. Japan* **72** 599–606

[9] Kamakura N, Takata Y, Tokushima T, Harada Y, Chainani A, Kobayashi K and Shin S 2006 *Phys. Rev.* B **74** 045127
[10] Tsui D C 1967 *Phys. Rev.* **164** 669–83
[11] Yang I, Savrasov S Y and Kotliar G 2001 *Phys. Rev. Lett.* **87** 216405
[12] von Barth U and Hedin L 1972 *J. Phys. C: Solid State Phys.* **5** 1629–42
[13] Wyckoff R W G 1963 *Crystal Structures* (New York: Wiley)
[14] Blöchl P E, Jepsen O and Andersen O K 1994 *Phys. Rev.* B **49** 16223–33
[15] Wakoh S, Tokii M, Matsumoto M and Matsumoto I 2002 *J. Phys. Soc. Japan* **71** 1393–400
[16] Koelling D D and Arbman G O 1975 *J. Phys. F: Met. Phys.* **5** 2041–54
[17] Hedin L 1965 *Phys. Rev.* **139** A796–823
[18] Kubo Y 2005 *J. Phys. Chem. Solids* **66** 2202–6
[19] Kubo Y 2004 *J. Phys. Chem. Solids* **65** 2077–82
[20] Yamasaki A and Fujiwara T 2003 *J. Phys. Soc. Japan* **72** 607–10